Field-driven domain wall motion in ferrimagnetic nanowires

K. Y. Jing [1], X. Gong [1], and X. R. Wang [1,2,3,*]

[1] *Physics Department, The Hong Kong University of Science and Technology, Clear Water Bay, Kowloon, Hong Kong, China*

[2] *HKUST Shenzhen Research Institute, Shenzhen 518057, China*

[3] *William Mong Institute of Nano Science and Technology, The Hong Kong University of Science and Technology, Clear Water Bay, Kowloon, Hong Kong, China*

(Received 9 June 2022; revised 11 November 2022; accepted 14 November 2022; published 22 November 2022)

Magnetic domain wall (DW) propagation in nanowires is an important problem whose applications require stable high speeds that are very difficult to achieve with ferromagnets due to the existence of the Walker breakdown, which separates a rigid-body motion from an oscillatory motion. One of the recent fascinating discoveries in magnetism is the high-speed DW motion along ferrimagnetic (FiM) nanowires near the angular momentum compensation point (AMCP). A clear understanding of this fascinating phenomenon is still lacking. Here we use the energy conservation principle and generic FiM dynamics to reveal the physics behind the DW motion and the absence of the Walker breakdown and precessional torque at the AMCP. An almost exact DW velocity formula beyond the Walker breakdown field is obtained that agrees with experiments and simulations. This theory provides useful guidance for the design of high-speed spintronic DW devices.

DOI: 10.1103/PhysRevB.106.174429

I. INTRODUCTION

Magnetic domain wall (DW) dynamics in nanowires has attracted much attention for its rich physics [1–5] and promising device applications such as racetrack memories [6]. One important goal in DW applications is the realization of high stable DW speed that requires a delay or removal of the Walker breakdown [7]. The endeavor of increasing DW velocity leads to the studies of DW motion in antiferromagnetic nanowires [8–10], and very recently, in ferrimagnetic (FiM) nanowires [11–27]. A ferrimagnet has at least two spin sublattices antiferromagnetically interacting with each other. It has two special states called the angular momentum compensation point (AMCP) at which the angular momenta of the two sublattices cancel each other, and the magnetization compensation point at which two magnetizations cancel each other. One class of ferrimagnets is rare-earth-transition-metal alloys whose AMCP and magnetization compensation point are different in general and can be tuned by compositions, other than the temperature. Unlike an antiferromagnet that is inert from external magnetic fields, FiM states provide a wider tunability and greater manipulability [11]. Also, unlike a ferromagnet, the net magnetization of a ferrimagnet can be very small but not zero, especially around an AMCP such that it is susceptible to the magnetic field with small Zeeman energy. The current understanding of experimentally observed very high DW speed of thousands of meters per second in compensated FiM nanowires near the AMCP [12–14] is from collective-coordinate approximation.

Although FiM dynamics should be described by partial differential equations for at least two sublattice magnetizations antiferromagnetically coupled, existing theories treat a FiM wire either as a ferromagnet whose dynamics follows Landau-Lifshitz-Gilbert (LLG) equation [13,14], or an antiferromagnet with the Néel order governed by a second-order partial differential equation [12,15,20,24–26]. DW dynamics is then obtained from converting the partial differential equations into ordinary differential equations for the collective coordinates of DW center and DW-plane canting angle [12,15,20,24–26]. Indeed, existing theories have enriched our understanding of DW dynamics in ferrimagnets in many aspects. However, these theories are based on the assumption that the DW structure must keep its spin profile during its motion. The assumption is surely valid below the Walker breakdown field. Beyond the breakdown, it is known that the DW plane precesses and the DW width oscillates, and in the case of a large transverse hard-axis anisotropy, spin wave emissions can accompany the DW propagation [1,2]. Also, the Thiele equation [28], based on collective-coordinate approximation, does not automatically explain the fascinating findings of DW motion in FiM nanowires. A unified theory, which works for the full range of magnetic field, is highly desired.

In this paper, the origin of high DW speed and absence of Walker breakdown field at the AMCP of a FiM nanowire are explained based on generic dynamics for coupled sublattice magnetizations of a ferrimagnet with a general Rayleigh dissipation. We show that a static DW between two domains with different energy densities does not exist. Spins in the DW must move in a field that creates such an energy density difference. Moving spins must dissipate energy due to the inevitable coupling between spins and their environment described by Gilbert damping in magnetization dynamics. The dissipated energy must be compensated by the Zeeman energy released from the DW propagation toward domain of the higher energy

*phxwan@ust.hk

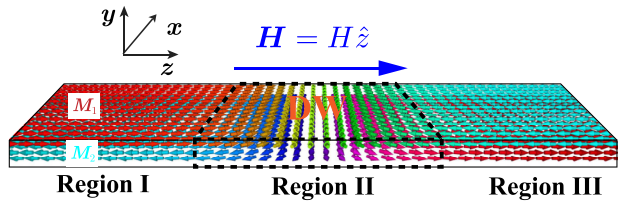

FIG. 1. Schematic of a head-to-head DW in a FiM nanowire. Region I and III are two uniform FiM domains, separated by a DW (region II) whose width is Δ. DW structure can be very complicated. $\boldsymbol{H}$ is the external field. Colors denote the spin orientations: red for spins along $\hat{z}$ and light blue for spins along $-\hat{z}$.

density. At the AMCP, precessional torque vanishes due to the zero angular momentum and the Walker breakdown field becomes infinity, leading to the high DW speed. Furthermore, a universal relationship between DW velocity and DW structure is obtained, and an almost exact formula for high-field DW velocity is derived, providing insight from the energy conservation principle.

II. MODEL

We consider a head-to-head DW in a FiM nanowire consisting of two antiferromagnetically interacting spin sublattices, whose easy axis is along the wire defined as the z axis as shown in Fig. 1. $\boldsymbol{M}_1$ and $\boldsymbol{M}_2$ are the magnetizations of the two sublattices, respectively. The total magnetic energy of the wire in the presence of a uniform magnetic field $\boldsymbol{H}$ is $E = \int \varepsilon \, d^3\boldsymbol{x}$ with the energy density of

$$\varepsilon = J\boldsymbol{M}_1 \cdot \boldsymbol{M}_2 + \sum_{\ell=1,2} [A_\ell (\nabla \boldsymbol{M}_\ell)^2 + f_\ell(\boldsymbol{M}_\ell) - \mu_0 \boldsymbol{M}_\ell \cdot \boldsymbol{H}], \tag{1}$$

where $J > 0$ is the antiferromagnetic inter-sublattice spin coupling constant. A_ℓ and f_ℓ are respectively the ferromagnetic exchange stiffness and magnetic anisotropic energy density of sublattice ℓ ($\ell = 1, 2$), μ_0 is the vacuum permeability. f_ℓ is assumed to have two equal minima at $\boldsymbol{M}_\ell = \pm M_\ell \hat{z}$.

The FiM magnetization dynamics is governed by the following equations [29,30]:

$$\begin{aligned}
\frac{1}{\gamma_1}\frac{\partial \boldsymbol{M}_1}{\partial t} &= -\boldsymbol{M}_1 \times \left(\boldsymbol{H}_1 - \frac{\alpha_{11}}{\gamma_1 M_1}\frac{\partial \boldsymbol{M}_1}{\partial t} - \frac{\alpha_{12}}{\gamma_1 M_1}\frac{\partial \boldsymbol{M}_2}{\partial t} \right), \\
\frac{1}{\gamma_2}\frac{\partial \boldsymbol{M}_2}{\partial t} &= -\boldsymbol{M}_2 \times \left(\boldsymbol{H}_2 - \frac{\alpha_{22}}{\gamma_2 M_2}\frac{\partial \boldsymbol{M}_2}{\partial t} - \frac{\alpha_{21}}{\gamma_2 M_2}\frac{\partial \boldsymbol{M}_1}{\partial t} \right),
\end{aligned} \tag{2}$$

where $\boldsymbol{H}_\ell = -\mu_0^{-1}\delta E/\delta \boldsymbol{M}_\ell$ and $\gamma_\ell = g_\ell \mu_B \mu_0/\hbar$ ($\ell = 1, 2$) are the effective field and the gyromagnetic ratio for $\boldsymbol{M}_\ell$, respectively. g_ℓ, μ_B, and $\hbar$ are the Landé g factor of sublattice ℓ ($\ell = 1, 2$), the Bohr magneton, and the Planck constant, respectively. α_{11}, α_{22} and α_{12}, α_{21} are intra-sublattice and inter-sublattice damping coefficients. We have $\alpha_{12}/\gamma_1 M_1 = \alpha_{21}/\gamma_2 M_2$ due to the action-reaction law. $s_\ell = M_\ell/\gamma_\ell$ is the spin density of sublattice ℓ ($\ell = 1, 2$). $\gamma_1 \neq \gamma_2$ in a general ferrimagnet because of the difference in Landé g factors of sublattices. For example, in GdFeCo alloys, $g_{\rm Gd} \simeq 2$, $g_{\rm FeCo} \simeq 2.2$ [12].

III. THEORETICAL RESULTS

We prove first that no static DW is allowed in the presence of a magnetic field along the z direction, except at the magnetization compensation point. If a static DW solution exists, the DW structure should satisfy equations $\boldsymbol{M}_\ell \times \boldsymbol{H}_\ell = 0$ ($\ell = 1, 2$). As proved in Appendix B, it implies $\boldsymbol{M}_\ell(\boldsymbol{x}, t)$ ($\ell = 1, 2$) satisfying following equation:

$$\oiint_{\partial\Omega} \left[\varepsilon \mathbb{1} - \sum_{\ell=1,2}^{i=x,y,z} 2A_\ell (\nabla M_{\ell,i}) \otimes (\nabla M_{\ell,i}) \right] \cdot d\boldsymbol{\sigma} = \text{const.}, \tag{3}$$

where $\partial\Omega$ is the surface of any chosen volume, $\mathbb{1}$ is the 3×3 unit matrix, and $\otimes$ denotes the dyadic product. Equation (3) cannot be true for a DW with $\boldsymbol{M}_1 = M_1\hat{z}, \boldsymbol{M}_2 = -M_2\hat{z}$ on its left and $\boldsymbol{M}_1 = -M_1\hat{z}, \boldsymbol{M}_2 = M_2\hat{z}$ on its right as shown in Fig. 1, or vice versa, because it requires $(M_1 - M_2)H = 0$. Thus, a static DW can only exist either with $H = 0$ or $M_1 = M_2$. In other words, a static DW cannot exist between two domains with different energy densities. This result can also be understood from the following argument: Assume $\boldsymbol{M}_\ell(\boldsymbol{x})$ is a static DW that separate a left domain with a lower energy density ε_1 from the right domain with a higher energy density $\varepsilon_2 (> \varepsilon_1)$. The energy change by shifting DW to the right by a distance L, i.e., $\boldsymbol{M}_\ell(\boldsymbol{x}) \to \boldsymbol{M}_\ell(\boldsymbol{x} - L\hat{z})$, is $LS(\varepsilon_1 - \varepsilon_2) < 0$, here S is the cross-section area of the wire. The DW is not stable against a rigid shift to the right because this small change in spin structure always lowers the system energy. Thus a DW must vary with time under a magnetic field.

When J is much larger than the Zeeman energy, $\boldsymbol{M}_1$ and $\boldsymbol{M}_2$ are always antiparallel to each other. We define $\boldsymbol{M}_{\rm eff} = (M_1 - M_2)\boldsymbol{m}$, where $\boldsymbol{m}$ is the unit vector of $\boldsymbol{M}_1$. Then $\boldsymbol{m}$ satisfies the following equation:

$$(s_1 - s_2)\frac{\partial \boldsymbol{m}}{\partial t} = -(M_1 - M_2)\boldsymbol{m} \times \boldsymbol{H}_{\rm eff} + \alpha \boldsymbol{m} \times \frac{\partial \boldsymbol{m}}{\partial t}, \tag{4}$$

where $\boldsymbol{H}_{\rm eff} = (M_1\boldsymbol{H}_1 - M_2\boldsymbol{H}_2)/(M_1 - M_2)$. In terms of $\boldsymbol{m}$, the total energy is $E[\boldsymbol{m}] = \int [A(\nabla \boldsymbol{m})^2 + f(\boldsymbol{m}) - \mu_0(M_1 - M_2)\boldsymbol{m} \cdot \boldsymbol{H}] d^3\boldsymbol{x}$ with $A = A_1 M_1^2 + A_2 M_2^2$, $f(\boldsymbol{m}) = f_1(M_1\boldsymbol{m}) + f_2(-M_2\boldsymbol{m})$. Denote $\alpha = \alpha_{11}s_1 + \alpha_{22}s_2 - \alpha_{12}s_2\frac{\gamma_2}{\gamma_1} - \alpha_{21}s_1\frac{\gamma_1}{\gamma_2}$, the thermodynamic second law requires $\alpha > 0$ to ensure the Rayleigh dissipation functional $\mathcal{R} = \frac{\mu_0 \alpha}{2}\int (\frac{\partial \boldsymbol{m}}{\partial t})^2 d^3\boldsymbol{x}$ [29–32] to be positive-definite. Equation (4) says that the change of spin angular momentum (left-hand side) equals the net torque (right-hand side) that is the sum of a torque from an effective field on the net magnetization ($M_1 - M_2 \neq 0$) and a dissipative torque from the motion of $\boldsymbol{m}$. At the AMCP, the dissipative torque cancels the field torque.

Equation (4) can be recast as an effective LLG equation [14,24,33–35],

$$\frac{\partial \boldsymbol{m}}{\partial t} = -\gamma_{\rm eff}\boldsymbol{m} \times \boldsymbol{H}_{\rm eff} + \alpha_{\rm eff}\boldsymbol{m} \times \frac{\partial \boldsymbol{m}}{\partial t}, \tag{5}$$

with an effective gyromagnetic ratio $\gamma_{\rm eff} = |M_1 - M_2|/(s_1 - s_2)$ and an effective Gilbert damping $\alpha_{\rm eff} = \alpha/(s_1 - s_2)$. $\gamma_{\rm eff}\alpha_{\rm eff}$ is always positive because a moving magnetization must dissipate its energy to its environment [see Eq. (6) below]. $s_1 > s_2$ and $s_1 < s_2$ correspond to sublattice-1 and sublattice-2 dominate cases. Following a similar derivation in

the literature [36], the energy dissipation rate is [37,38]

$$\frac{dE}{dt} = -\frac{\alpha_{\rm eff}\gamma_{\rm eff}\mu_0}{(1+\alpha_{\rm eff}^2)(M_1-M_2)}\int (\boldsymbol{M}_{\rm eff}\times\boldsymbol{H}_{\rm eff})^2 d^3\boldsymbol{x}. \quad (6)$$

We divide the wire into three regions as shown in Fig. 1: I for the domain with $\boldsymbol{M}_{\rm eff}$ parallel to $\boldsymbol{H}$, II for the DW, and III for the domain with $\boldsymbol{M}_{\rm eff}$ antiparallel to $\boldsymbol{H}$. Energy dissipation occurs only in the DW region (region II) where $\boldsymbol{M}_{\rm eff}$ and $\boldsymbol{H}_{\rm eff}$ are not collinear [37,38]. The change rate of energies, $E_{\rm I}$ and $E_{\rm III}$, of region I and III comes from the DW propagation along the wire, and should be $\frac{d(E_{\rm I}+E_{\rm III})}{dt} = -2\mu_0(M_1-M_2)Hv S$, where v is the DW velocity. DW energy $E_{\rm II}$ must be around a certain value. Thus the time-averaged energy change rate must be zero. In another word, $dE_{\rm II}/dt$ is either zero or oscillates with zero average. The energy conservation requires

$$v = \frac{\alpha_{\rm eff}\gamma_{\rm eff}}{2HS(1+\alpha_{\rm eff}^2)}\int (\boldsymbol{m}\times\boldsymbol{H}_{\rm eff})^2 d^3\boldsymbol{x} + \frac{1}{2\mu_0(M_1-M_2)HS}\frac{dE_{\rm II}}{dt}. \quad (7)$$

This is a universal relationship between DW velocity and the DW structure and can serve as a proper definition of instantaneous DW velocity. The second term on the right-hand side should be identically zero in the case of a rigid DW motion such that the DW velocity is constant. In the case that a DW deforms itself during its propagation, the energy dissipation rate and DW energy $E_{\rm II}$ oscillates with time and $\overline{\frac{dE_{\rm II}}{dt}} = 0$, where the bar denotes the time average. This results in an oscillatory DW speed whose time-averaged value is

$$\bar{v} = \frac{\alpha_{\rm eff}\gamma_{\rm eff}}{2HS(1+\alpha_{\rm eff}^2)}\overline{\int (\boldsymbol{m}\times\boldsymbol{H}_{\rm eff})^2 d^3\boldsymbol{x}}. \quad (8)$$

We note $(\boldsymbol{m}\times\boldsymbol{H}_{\rm eff})^2 = H_{{\rm eff},\theta}^2 + H_{{\rm eff},\phi}^2$, where $H_{{\rm eff},\theta}$ and $H_{{\rm eff},\phi}$ are two field components perpendicular to $\boldsymbol{m}$ in the local coordinate framework $(\boldsymbol{e}_{\boldsymbol{m}}, \boldsymbol{e}_\theta, \boldsymbol{e}_\phi)$. $\theta(\boldsymbol{x},t)$ and $\phi(\boldsymbol{x},t)$ are the polar and the azimuthal angles of $\boldsymbol{m}$. $H_{{\rm eff},\theta}$ and $H_{{\rm eff},\phi}$ are given by

$$\begin{aligned} H_{{\rm eff},\theta} &= -H\sin\theta + G, \\ H_{{\rm eff},\phi} &= -\frac{1}{\mu_0(M_1-M_2)\sin\theta}\frac{\partial f}{\partial\phi} + \frac{2A}{\mu_0(M_1-M_2)\sin\theta}\frac{\partial}{\partial z}\left(\sin^2\theta\frac{\partial\phi}{\partial z}\right), \end{aligned} \quad (9)$$

where $G = \frac{1}{\mu_0(M_1-M_2)}[2A\frac{\partial^2\theta}{\partial z^2} - \frac{\partial f}{\partial\theta} - 2A\sin\theta\cos\theta(\frac{\partial\phi}{\partial z})^2]$. Equation (5) along $\boldsymbol{e}_\theta, \boldsymbol{e}_\phi$ becomes

$$\begin{aligned} \frac{\partial\theta}{\partial t} &= \gamma_{\rm eff}H_{{\rm eff},\phi} - \alpha_{\rm eff}\sin\theta\frac{\partial\phi}{\partial t} \\ \sin\theta\frac{\partial\phi}{\partial t} &= -\gamma_{\rm eff}H_{{\rm eff},\theta} + \alpha_{\rm eff}\frac{\partial\theta}{\partial t}. \end{aligned} \quad (10)$$

Eliminating time-derivative of θ from Eq. (10), we have

$$(1+\alpha_{\rm eff}^2)\sin\theta\frac{\partial\phi}{\partial t} = \gamma_{\rm eff}(\alpha_{\rm eff}H_{{\rm eff},\phi} - H_{{\rm eff},\theta}). \quad (11)$$

If the DW propagates as a rigid-body along the z direction, in the case of a field below the Walker breakdown [7], i.e., $\frac{\partial\phi}{\partial z} = 0$, $\frac{\partial^2\phi}{\partial z^2} = 0$, and $\frac{\partial\phi}{\partial t} = 0$, using Eq. (9), we have $2A\frac{\partial^2\theta}{\partial z^2} - \frac{\partial f}{\partial\theta} = 0$, so that $H_{{\rm eff},\theta} = -H\sin\theta$, whose maximal allowed external field is the Walker breakdown field. For $(M_1-M_2), (s_1-s_2) \neq 0$, $\frac{\partial\phi}{\partial t} = 0$ obviously requires $\alpha_{\rm eff}H_{{\rm eff},\phi} = H_{{\rm eff},\theta}$. This means that the DW-plane cants an angle to generate a nonzero $H_{{\rm eff},\phi}$ to coherently vary θ such that the DW propagates along the wire. Below we consider a biaxial model of magnetic anisotropy $f(\theta,\phi) = -K_z\cos^2\theta + K_y\sin^2\theta\sin^2\phi$, the Walker breakdown field is $H_W = \max(\frac{\alpha_{\rm eff}K_y\sin 2\phi}{\mu_0(M_1-M_2)}) = \frac{\alpha K_y}{\mu_0|(M_1-M_2)(s_1-s_2)|}$. Both $\gamma_{\rm eff}$ and $\alpha_{\rm eff}$ diverge as $(s_1-s_2)^{-1}$ near the AMCP. The limit of Eq. (11) under $s_1-s_2\to 0$ ($\alpha_{\rm eff}^2, \gamma_{\rm eff}\alpha_{\rm eff} \sim (s_1-s_2)^{-2}$) gives $H_{{\rm eff},\phi} = 0$ and $\phi = 0$ when $\frac{\partial\phi}{\partial t} = 0$. Thus the DW plane remains in the xz plane and never rotates, leading to an infinite H_W at the AMCP. One can also see this point by considering an equivalent form of Eq. (5), $\frac{\partial\boldsymbol{m}}{\partial t} = -\frac{\gamma_{\rm eff}}{1+\alpha_{\rm eff}^2}\boldsymbol{m}\times\boldsymbol{H}_{\rm eff} - \frac{\gamma_{\rm eff}\alpha_{\rm eff}}{1+\alpha_{\rm eff}^2}\boldsymbol{m}\times(\boldsymbol{m}\times\boldsymbol{H}_{\rm eff})$. At the AMCP, the precessional torque vanishes since $\frac{\gamma_{\rm eff}}{1+\alpha_{\rm eff}^2}\to 0$ as $(s_1-s_2)\to 0$ while the damping torque is finite because of $\lim_{(s_1-s_2)\to 0}\frac{\gamma_{\rm eff}\alpha_{\rm eff}}{1+\alpha_{\rm eff}^2} = \frac{(M_1-M_2)}{\alpha} \neq 0$. This means that the precessional motion is completely prohibited, and $\boldsymbol{m}$ at any point inside the DW rotates coherently toward external field, leading to a rigid DW propagation along the wire.

Equation (5) with our biaxial magnetic anisotropy has the well-known Walker DW solution [7] of $\theta(z,t) = 2\arctan\{\exp[(z-\int_0^t v(\tau)d\tau)/\Delta(t)]\}$, where Δ is the DW width. It gives $\frac{dE_{\rm II}}{dt} = -\frac{4AS}{\Delta^2}\frac{d\Delta}{dt} = 0$ for a rigid-body DW propagation. $H_{{\rm eff},\theta} = \alpha_{\rm eff}H_{{\rm eff},\phi} = -H\sin\theta$, $(\boldsymbol{m}\times\boldsymbol{H}_{\rm eff})^2 = H_{{\rm eff},\theta}^2 + H_{{\rm eff},\phi}^2 = (1+\alpha_{\rm eff}^2)H^2\sin^2\theta/\alpha_{\rm eff}^2$. Substituting DW width definition of $\int\sin^2\theta d^3\boldsymbol{x} = 2S\Delta$ into equation (7), one has $v = \frac{(M_1-M_2)\Delta}{\alpha}H$ and DW speed at Walker breakdown field $v_W = \frac{K_y\Delta}{\mu_0(s_1-s_2)}$, independent of the damping coefficient and divergent at the AMCP.

Away from the AMCP, H_W is finite. A DW shall precess around wire axis during its propagation along the wire when $H > H_W$. From Eqs. (8) and (9), we have the average DW velocity (see Appendix C for detailed derivation)

$$\bar{v} = c_1 H + \frac{c_1}{\alpha_{\rm eff}^2}\left(H - \sqrt{H^2 - H_W^2}\right), \quad (12)$$

where $c_1 = \frac{\alpha_{\rm eff}\gamma_{\rm eff}}{2S(1+\alpha_{\rm eff}^2)}\overline{\int\sin^2\theta d^3\boldsymbol{x}} = \frac{(M_1-M_2)\alpha\bar{\Delta}}{(s_1-s_2)^2+\alpha^2}$ is peaked at the AMCP. Equation (12) is exact under very sensible assumptions, and all coefficients in Eq. (12) are fully determined by the model parameters. Equation (12) predicts a negative differential DW mobility in the range of $H_W < H < \frac{\alpha_{\rm eff}^2+1}{\sqrt{\alpha_{\rm eff}^4+2\alpha_{\rm eff}^2}}H_W$. This prediction is also true for ferromagnetic case.

Figure 2 illustrates three types of DW motion. For $H < H_W$, the DW plane cants a fixed angle ϕ and propagate rigidly along the wire at a constant velocity such that the damping torque cancels the torque from the applied field along the wire, as shown in Fig. 2(a). Energy dissipation comes from the unbalanced transverse (to the wire) field that causes coherent

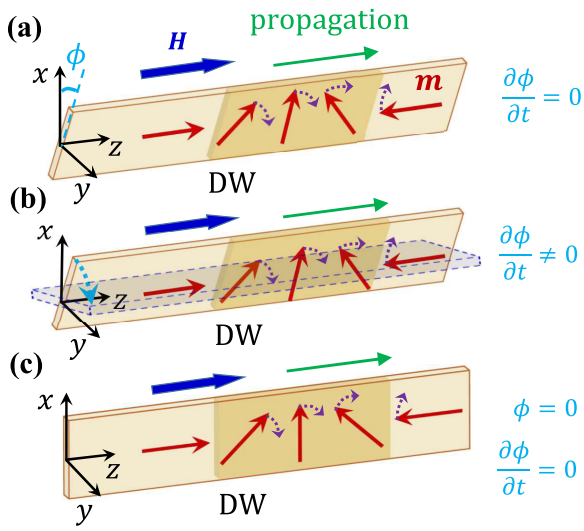

FIG. 2. Illustration of three types of DW motions. (a) $H < H_W$ ($s_1 \neq s_2$), the DW plane cants an angle ϕ and the DW propagates rigidly along the wire at a constant velocity. (b) $H > H_W$ ($s_1 \neq s_2$), the DW plane precesses around wire axis during DW propagation along the wire. (c) At the AMCP, the DW plane does not cant and stay in the x-z plane (initial configuration). The red, blue, green, and purple arrows denote $\boldsymbol{m}$, magnetic field, DW propagation direction, and DW plane precession, respectively.

spin rotation inside the DW (the dashed violet arrows) to facilitate DW propagation along the wire. For $H > H_W$ ($s_1 \neq s_2$) as shown in Fig. 2(b), the DW plane precesses around wire axis (the dashed light-blue arrows) during DW propagation along the wire. In this mode, part of the applied field is unbalanced (by damping torque) and provides a torque to rotate the DW plane around the wire. The unbalanced transverse field due to the transverse anisotropy provides a torque to coherently rotate spins inside the DW (the dashed violet arrows). DW velocity oscillates with time. Figure 2(c) is for $s_1 = s_2$. The precessional torque is absent as explained above, and only nonzero dissipative torque exists under an applied field. Thus the DW always undergoes a rigid-body motion no matter how large the external field is as long as the field does not destroy the DW structure, or $H_W = \infty$. The net field provides coherent spin rotation (the dashed violet arrows) such that the DW propagates rigidly along the wire. This explains the high DW speeds observed in FiM wires at the AMCP.

IV. MICROMAGNETIC SIMULATIONS

In order to find out how accurate of Eq. (12) is for $H > H_W$, we use MuMax3 [39] to numerically solve Eq. (2) for synthetic FiM strip wires [40] as shown in Fig. 1 that consist of two antiferromagnetically coupled ferromagnetic layers of 1nm thick each. Different layers represent different sublattices, thus the sublattice index ℓ is also used as layer index. The strip size is $16\,\text{nm} \times 2\,\text{nm} \times 1024\,\text{nm}$. The cell size in simulations is chosen to be $1\,\text{nm} \times 1\,\text{nm} \times 1\,\text{nm}$. To mimic a rare-earth-transition-metal alloy (such as GdFeCo, GdFe, GdCo) [12,13,15,18,41–44] the model parameters are $J = 1.2 \times 10^{-4}\,\text{J A}^{-2}\text{m}^{-1}$, $A_1 = 9.8 \times 10^{-24}\,\text{J m A}^{-2}$, $A_2 = 1.23 \times 10^{-23}\,\text{J m A}^{-2}$, biaxial anisotropies are considered for each layer, $f_\ell = -\frac{K_{\ell,z}}{M_\ell^2} M_{\ell,z}^2 + \frac{K_{\ell,y}}{M_\ell^2} M_{\ell,y}^2$, $\ell = 1, 2$, $K_{1,z} = K_{2,z} = 0.65\,\text{MJ/m}^3$, $\alpha_{12} = \alpha_{21} = 0$. $K_{\ell,y}$ and $\alpha_{\ell\ell}$ ($\ell = 1, 2$) are used for simulating different systems as labeled by Set 1–6 in Table I. Note that $K_z = K_{1,z} + K_{2,z}$, $K_y = K_{1,y} + K_{2,y}$. The gyromagnetic ratios are $\gamma_1 = \gamma_2 = 1.76 \times 10^{11}\,\mu_0\,\text{s}^{-1}\text{T}^{-1}$ except for the AMCP case, the saturation magnetizations are $M_1 = 1010\,\text{kA/m}$, $M_2 = 900\,\text{kA/m}$. The coupling field between two sublattices is of hundreds of Tesla to guarantee the collinearity of two spin sublattices. Different from a natural ferrimagnet, inter-sublattice coupling is only along the y direction in our synthetic ferrimagnet. To simulate the AMCP, we take $\gamma_2 = 1.76 \times 10^{11}\,\mu_0\,\text{s}^{-1}\text{T}^{-1}$ and $\gamma_1 = 1.975 \times 10^{11}\,\mu_0\ \text{s}^{-1}\text{T}^{-1}$ such that $M_1/\gamma_1 = M_2/\gamma_2$ and the net angular momentum is zero. All other parameters remain unchanged. Although MuMax3 does not allow to set different gyromagnetic ratios for different FM layers directly, this $\gamma_1 \neq \gamma_2$ case can be realized by rescaling the effective field in layer 1 ($\boldsymbol{H}_1$) with a factor γ_1/γ_2. The reason is that the dynamical equation $\frac{\partial \boldsymbol{M}_1}{\partial t} = -\gamma_1 \boldsymbol{M}_1 \times \boldsymbol{H}_1 + \frac{\alpha_{11}}{M_1} \boldsymbol{M}_1 \times \frac{\partial \boldsymbol{M}_1}{\partial t}$ is equivalent to $\frac{\partial \boldsymbol{M}_1}{\partial t} = -\gamma_2 \boldsymbol{M}_1 \times (\frac{\gamma_1}{\gamma_2} \boldsymbol{H}_1) + \frac{\alpha_{11}}{M_1} \boldsymbol{M}_1 \times \frac{\partial \boldsymbol{M}_1}{\partial t}$.

In the simulation, a DW is first created at the center of nanowire, then a uniform magnetic field is applied in the $+\hat{z}$ direction. The velocity is obtained from the linear fit of time-evolution curve of the DW center (where $m_z = 0$). For fields above the Walker breakdown, the average velocities are obtained from data accumulated for more than 4 velocity oscillating periods.

We consider six different systems with various $K_{\ell,y}$ and $\alpha_{\ell\ell}$ ($\ell = 1, 2$). The detail values of the model parameters are given in Table I. Because of large velocity difference, Fig. 3(a) plot $\bar{v}$ vs $\mu_0 H$ for three systems with the same $\alpha_{\ell\ell} = 0.02$ and

TABLE I. $K_{y,1}$, $K_{y,2}$, α_{11}, and α_{22} are model parameters. α_{eff}, K_y, $\mu_0 H_W$, $\bar{\Delta}$, and c_1 are computed quantities.

Data set	Set 1	Set 2	Set 3	Set 4	Set 5	Set 6
$K_{1,y}$ (MJ/m^3)	0.05	0.035	0.02	0.1	0.1	0.1
$K_{2,y}$ (MJ/m^3)	0.05	0.035	0.02	0.1	0.1	0.1
α_{11}	0.02	0.02	0.02	0.005	0.01	0.015
α_{22}	0.02	0.02	0.02	0.005	0.01	0.015
α_{eff}	0.3473	0.3473	0.3473	0.0868	0.1736	0.2605
K_y (MJ/m^3)	0.1	0.07	0.04	0.2	0.2	0.2
$\mu_0 H_W$ (T)	0.3157	0.2210	0.1263	0.1579	0.3157	0.4736
$\bar{\Delta}$ (nm)	3.85	3.87	3.89	3.79	3.75	3.79
c_1 (μ_0 m $\text{s}^{-1}\text{T}^{-1}$)	210.00	211.13	212.34	57.48	111.37	162.69

different $K_{\ell,y}$, label as Set 1, 2, 3. Figure 3(b) is the similar plots for three systems with the same $K_{\ell,y} = 0.1\,\mathrm{MJ/m^3}$, but different $\alpha_{\ell\ell}$, label as Set 4, 5, 6. The corresponding values of c_1, α_{eff}, and H_W computed from this theory are also given in Table I. The perfect agreement between the simulation results (the symbols) and theoretical prediction (the solid curves) demonstrates that Eq. (12) is almost exact. The insets are DW velocities at the AMCP obtained from simulations (symbols), and from theoretical prediction $v = \frac{(M_1-M_2)\Delta}{\alpha} H$ (the solid lines), which accords well with the simulations without any fitting parameter. No Walker breakdown phenomena occurs at the AMCP, as explained in Sec. III.

V. DISCUSSION AND CONCLUSIONS

Before conclusion, we would like to make a few remarks. (1) The relationship between the instantaneous DW velocity and the DW structure is exact that explains why our high-field DW velocity formula without any fitting parameters agrees perfectly with simulation results. (2) The theory is applicable to all types of DWs since no collective-mode approximation is used. (3) High DW velocity is a result of the absence of the Walker breakdown field at the AMCP. This explains the observed high DW speed of more than 1.5 km/s at the AMCP although the mobility $\mu = \frac{(M_1-M_2)\Delta}{\alpha}$ for $H < H_W$ itself is comparable to or even smaller than that for a ferromagnetic wire [45,46]. (4) The general principle presented in this paper should be applicable to all kinds of magnetic spin texture whose dynamics are governed by LLG-like equation(s). Thus, it is prospective to describe the dynamics of other spin textures (such as skyrmions) using our approach.

In summary, a generic theory of field-driven DW motion in FiM wires is presented. A static DW cannot exist in a homogeneous ferrimagnetic nanowire when a uniform static magnetic field or any other external force creates an energy density difference between two domains separated by the DW. Spins in the DW must vary with time under the external magnetic field such that the system energy is dissipated due to the Gilbert damping. The dissipated energy must be compensated by the Zeeman energy released from moving the DW toward the domain with the higher energy density. High DW speed near the AMCP is the consequence of the absence of precessional torque and infinite high Walker breakdown field at the AMCP. A lower Zeeman energy density and a high energy dissipation rate contribute also to the high DW speed at a reasonably lower field near the AMCP. Away from the AMCP, our approach can not only obtain the exact DW velocity below the Walker breakdown field, but also an almost exact velocity formula beyond the Walker breakdown field. This theory agrees with all existing experiments [12,15,18], simulations, and provides useful guidance to DW manipulation and opens an avenue for designing high-speed spintronic devices.

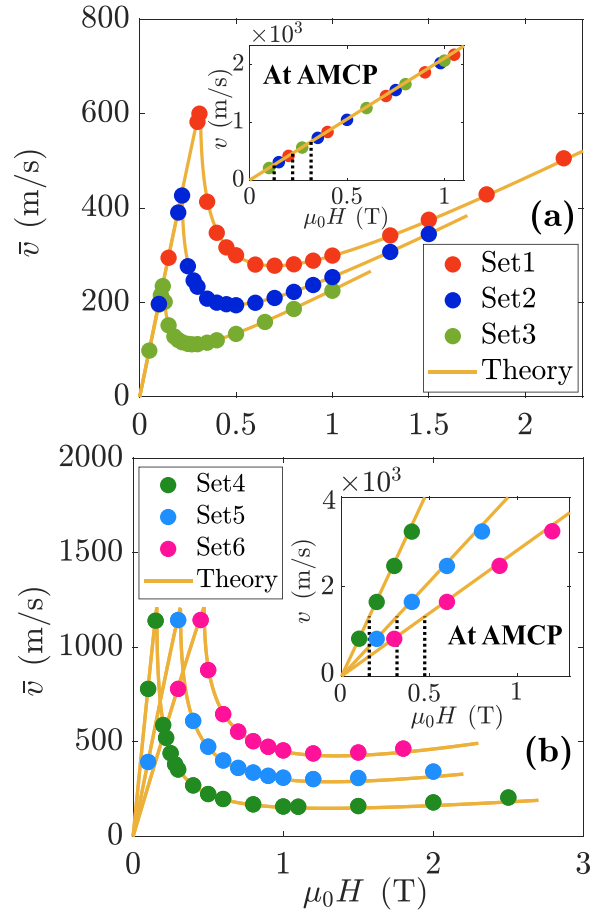

FIG. 3. Average DW velocity of a head-to-head DW as a function of applied field along the $+\hat{z}$ direction. Symbols are MuMax3 simulation results and solid curves are theoretical formula without any fitting parameter. (a) Three systems (denoted as Set 1, 2, 3) with the same $\alpha_{11} = \alpha_{22} = 0.02$ but different $K_{\ell,y}$. (b) Three systems (denoted as Set 4, 5, 6) with the same $K_{\ell,y} = 0.1\,\mathrm{MJ/m^3}$ but different $\alpha_{\ell\ell}$ ($\ell = 1, 2$). Their values are listed in Table I. The insets are DW velocities at AMCP ($M_1/\gamma_1 = M_2/\gamma_2$) with all other parameters unchanged. The black-dashed lines indicate the Walker breakdown fields in the main figures.

ACKNOWLEDGMENTS

K.Y.J. thanks J. Sampaio for useful help on micromagnetic simulations at AMCP. This work is supported by the National Key Research and Development Program of China Grant No. 2020YFA0309600, the National Natural Science Foundation of China (Grant No. 11974296) and Hong Kong RGC Grants (No. 16301518, No. 16301619, No. 16302321, and No. 16300522).

APPENDIX A: ENERGY DISSIPATION RATE AND RAYLEIGH DISSIPATION FUNCTIONAL

It has been proved in Refs. [29,30] that a general Rayleigh dissipation functional $\mathcal{R}$ for FiM magnetization dynamics takes form of

$$\mathcal{R}(\dot{\boldsymbol{M}}_1, \dot{\boldsymbol{M}}_2) = \mu_0 \int \left(\frac{\alpha_{11}\dot{\boldsymbol{M}}_1 \cdot \dot{\boldsymbol{M}}_1}{2\gamma_1 M_1} + \frac{\alpha_{22}\dot{\boldsymbol{M}}_2 \cdot \dot{\boldsymbol{M}}_2}{2\gamma_2 M_2} + \frac{\alpha_{12}\dot{\boldsymbol{M}}_1 \cdot \dot{\boldsymbol{M}}_2}{\gamma_1 M_1} \right) d^3\boldsymbol{x}, \tag{A1}$$

which gives rise to the damping torques in Eq. (2) in the main text. The dots denote time derivatives. Under the approximation that $\boldsymbol{M}_1$ and $\boldsymbol{M}_2$ are always antiparallel to each other, the

Rayleigh dissipation functional becomes

$$\mathcal{R} = \frac{\mu_0 \alpha}{2} \int \left(\frac{\partial \boldsymbol{m}}{\partial t} \right)^2 d^3\boldsymbol{x}, \tag{A2}$$

where $\alpha = \alpha_{11} s_1 + \alpha_{22} s_2 - \alpha_{12} s_2 \frac{\gamma_2}{\gamma_1} - \alpha_{21} s_1 \frac{\gamma_1}{\gamma_2}$. Using an equivalent form of Eq. (5) in the main text,

$$\frac{\partial \boldsymbol{m}}{\partial t} = -\frac{\gamma_{\text{eff}}}{1+\alpha_{\text{eff}}^2} \boldsymbol{m} \times \boldsymbol{H}_{\text{eff}} - \frac{\gamma_{\text{eff}} \alpha_{\text{eff}}}{1+\alpha_{\text{eff}}^2} \boldsymbol{m} \times (\boldsymbol{m} \times \boldsymbol{H}_{\text{eff}}), \tag{A3}$$

one can derive the energy dissipation rate of $\frac{dE}{dt} = -2\mathcal{R}$ [47],

$$\begin{aligned} \frac{dE}{dt} &= -\mu_0 \alpha \int \left(\frac{\partial \boldsymbol{m}}{\partial t} \right)^2 d^3\boldsymbol{x} \\ &= -\frac{\mu_0 \alpha \gamma_{\text{eff}}^2}{1+\alpha_{\text{eff}}^2} \int (\boldsymbol{m} \times \boldsymbol{H}_{\text{eff}})^2 d^3\boldsymbol{x} \\ &= -\frac{\alpha_{\text{eff}} \gamma_{\text{eff}} \mu_0}{(1+\alpha_{\text{eff}}^2)(M_1 - M_2)} \int (\boldsymbol{M}_{\text{eff}} \times \boldsymbol{H}_{\text{eff}})^2 d^3\boldsymbol{x}. \end{aligned} \tag{A4}$$

This is the same as Eq. (6) in the main text. Noting that $\boldsymbol{m} \times \boldsymbol{H}_{\text{eff}} \perp \boldsymbol{m} \times (\boldsymbol{m} \times \boldsymbol{H}_{\text{eff}})$, $(\boldsymbol{m} \times (\boldsymbol{m} \times \boldsymbol{H}_{\text{eff}}))^2 = (\boldsymbol{m} \times \boldsymbol{H}_{\text{eff}})^2$. In the last step, we have used the definition of effective parameters, $\gamma_{\text{eff}} = (M_1 - M_2)/(s_1 - s_2)$, $\alpha_{\text{eff}} = \alpha/(s_1 - s_2)$, and $\boldsymbol{M}_{\text{eff}} = (M_1 - M_2)\boldsymbol{m}$.

APPENDIX B: DERIVATION OF EQ. (3) IN THE MAIN TEXT

A static DW structure is a stable spin texture of $\boldsymbol{M}_\ell$, $\ell = 1, 2$, separating two domains. Our magnetic energy is $E = \int \varepsilon \, d^3\boldsymbol{x}$ with the energy density of

$$\begin{aligned} \varepsilon =& J\boldsymbol{M}_1 \cdot \boldsymbol{M}_2 + A_1 (\nabla \boldsymbol{M}_1)^2 + A_2 (\nabla \boldsymbol{M}_2)^2 + f_1(\boldsymbol{M}_1) \\ &+ f_2(\boldsymbol{M}_2) - \mu_0 (\boldsymbol{M}_1 + \boldsymbol{M}_2) \cdot \boldsymbol{H}. \end{aligned} \tag{B1}$$

In terms of polar and azimuthal angles, $\boldsymbol{M}_\ell = M_\ell(\sin\theta_\ell \cos\phi_\ell, \sin\theta_\ell \sin\phi_\ell, \cos\theta_\ell)$, $\ell = 1, 2$, the energy density becomes $\varepsilon = JM_1M_2[\sin\theta_1 \sin\theta_2 \cos(\phi_1 - \phi_2) + \cos\theta_1 \cos\theta_2] + A_1 M_1^2 [(\nabla\theta_1)^2 + \sin^2\theta_1 (\nabla\phi_1)^2] + A_2 M_2^2 [(\nabla\theta_2)^2 + \sin^2\theta_2 (\nabla\phi_2)^2] + f_1(\theta_1, \phi_1) + f_2(\theta_2, \phi_2) - \mu_0 M_1 H \cos\theta_1 - \mu_0 M_2 H \cos\theta_2$. Stable spin structures satisfy following partial differential equations:

$$\frac{\delta E}{\delta \theta_\ell} = \frac{\partial \varepsilon}{\partial \theta_\ell} - \nabla \cdot \frac{\partial \varepsilon}{\partial (\nabla \theta_\ell)} = 0, \tag{B2}$$

$$\frac{\delta E}{\delta \phi_\ell} = \frac{\partial \varepsilon}{\partial \phi_\ell} - \nabla \cdot \frac{\partial \varepsilon}{\partial (\nabla \phi_\ell)} = 0. \tag{B3}$$

Eq. (B2) $\times \nabla\theta_\ell +$ Eq. (B3) $\times \nabla\phi_\ell$ and summing over ℓ, one has

$$\begin{aligned} \sum_{\ell=1,2} \Bigg\{ & \frac{\partial \varepsilon}{\partial \theta_\ell} \nabla\theta_\ell - \left[\nabla \cdot \frac{\partial \varepsilon}{\partial (\nabla\theta_\ell)} \right] \nabla\theta_\ell + \frac{\partial \varepsilon}{\partial \phi_\ell} \nabla\phi_\ell \\ & - \left[\nabla \cdot \frac{\partial \varepsilon}{\partial (\nabla\phi_\ell)} \right] \nabla\phi_\ell \Bigg\} = \nabla \cdot \overleftrightarrow{T} = 0, \end{aligned} \tag{B4}$$

where $\overleftrightarrow{T} = \varepsilon \mathbb{1} - \sum_\ell 2A_\ell M_\ell^2 (\nabla\theta_\ell \otimes \nabla\theta_\ell + \sin^2\theta_\ell \nabla\phi_\ell \otimes \nabla\phi_\ell)$, or $\overleftrightarrow{T} = \varepsilon \mathbb{1} - \sum_{\ell=1,2}^{i=x,y,z} 2A_\ell (\nabla M_{\ell,i}) \otimes (\nabla M_{\ell,i})$. Here, $\mathbb{1}$ is the 3×3 unit matrix, and $\otimes$ denotes the dyadic product. Equation (B4) can also be recast as Eq. (3) in the main text, $\oiint_{\partial\Omega} \overleftrightarrow{T} \cdot d\boldsymbol{\sigma} = \text{const.}$, where $\partial\Omega$ is the closed surface of an arbitrarily chosen volume in the system, $d\boldsymbol{\sigma}$ is the differential area on $\partial\Omega$ pointing normally outward of the enclosed space. For a $\partial\Omega$ intercepting domains on the both side of a DW, this requires energy densities in the two domains to be equal, i.e., $(M_1 - M_2)H = 0$. Thus, a static DW can only exist when $H = 0$ or $M_1 = M_2$.

APPENDIX C: DERIVATION OF HIGH-FIELD AVERAGE DW VELOCITY

In this Appendix, we derive the averaged DW velocity of Eq. (12) in the main text for $H > H_W$.

1. Averaged DW velocity and effective fields

We start from Eq. (8) in the main text

$$\bar{v} = \frac{\alpha_{\text{eff}} \gamma_{\text{eff}}}{2HS(1+\alpha_{\text{eff}}^2)} \overline{\int (\boldsymbol{m} \times \boldsymbol{H}_{\text{eff}})^2 d^3\boldsymbol{x}}. \tag{C1}$$

Since

$$\overline{\int (\boldsymbol{m} \times \boldsymbol{H}_{\text{eff}})^2 d^3\boldsymbol{x}} = \overline{\int \left(H_{\text{eff},\theta}^2 + H_{\text{eff},\phi}^2 \right) d^3\boldsymbol{x}}, \tag{C2}$$

and from Eq. (9) of the main text, we have, by substituting above expressions into Eq. (C1),

$$\bar{v} = \frac{\alpha_{\text{eff}} \gamma_{\text{eff}}}{2HS(1+\alpha_{\text{eff}}^2)} \overline{\int \left(H^2 \sin^2\theta - 2GH \sin\theta + G^2 + H_{\text{eff},\phi}^2 \right) d^3\boldsymbol{x}}. \tag{C3}$$

Equation (C3) can be recast as

$$\bar{v} = c_1 H - \frac{c_1}{\bar{\Delta}} \overline{\int G \sin\theta \, dz} + \frac{c_1}{2\bar{\Delta}H} \overline{\int G^2 dz} + \frac{c_1}{2\bar{\Delta}H} \overline{\int H_{\text{eff},\phi}^2 dz}, \tag{C4}$$

where

$$c_1 = \frac{\alpha_{\text{eff}} \gamma_{\text{eff}}}{2S(1+\alpha_{\text{eff}}^2)} \overline{\int \sin^2\theta \, d^3\boldsymbol{x}} = \frac{\alpha_{\text{eff}} \gamma_{\text{eff}} \bar{\Delta}}{(1+\alpha_{\text{eff}}^2)} = \frac{(M_1 - M_2)\alpha \bar{\Delta}}{(s_1 - s_2)^2 + \alpha^2}. \tag{C5}$$

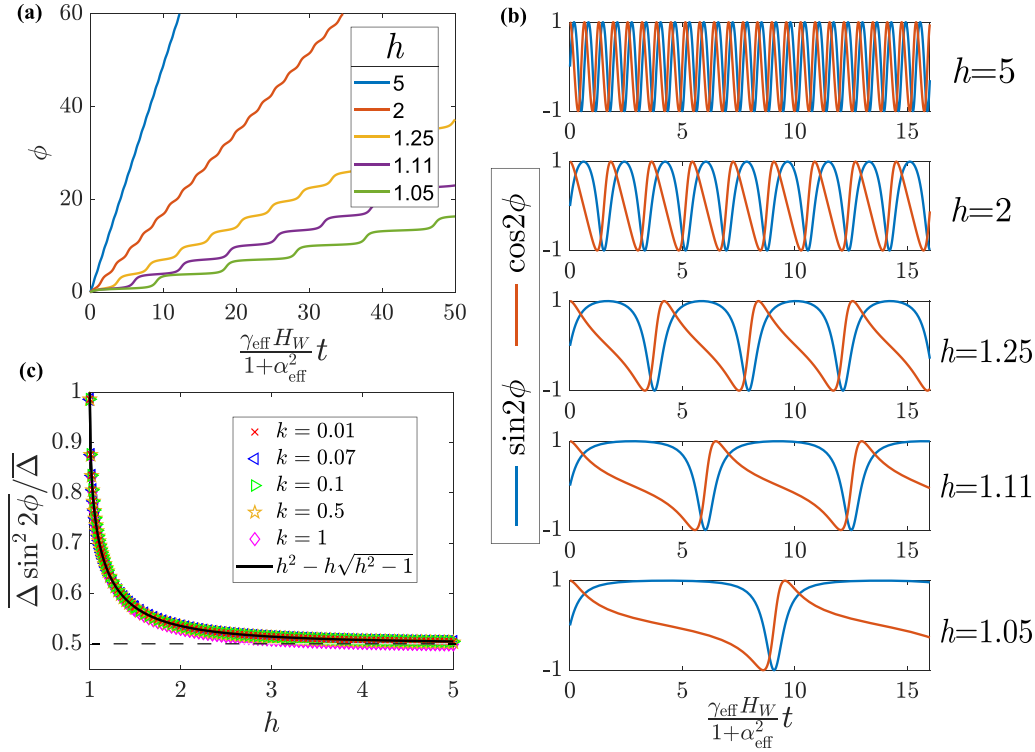

FIG. 4. (a) $\phi(t)$ curve of Eq. (C11) for various $h \equiv H/H_W$. (b) $\sin 2\phi(t)$ and $\cos 2\phi(t)$ computed from $\phi(t)$ in (a). (c) Field-dependence of $\frac{\overline{\Delta \sin^2 2\phi}}{\bar{\Delta}}$ obtained from numerical integrations (symbols) and $h^2 - h\sqrt{h^2-1}$ of Eq. (C12) (the solid curve).

DW width definition of $2S\Delta = \int \sin^2\theta d^3\boldsymbol{x}$ is used above. Equation (C4) is an exact expression for $\bar{v}$, depending on H and internal fields of G and $H_{\text{eff},\phi}$.

2. Estimation of G and $\overline{\int H_{\text{eff},\phi}^2 dz}$

To find the explicit field-dependence of $\bar{v}$, we consider a biaxial model of magnetic anisotropy $f = -K_z \cos^2\theta + K_y \sin^2\theta \sin^2\phi$. For this model, $\frac{\partial f}{\partial \theta} = 2\sin\theta\cos\theta(K_z + K_y \sin^2\phi)$, $\frac{\partial f}{\partial \phi} = K_y \sin^2\theta \sin 2\phi$. The integrals in Eq. (C4) depends on the DW structure, in order to estimate them, we need to make several assumptions, which are verified by micromagnetic simulations later in Appendix D. (1) $\theta(z,t)$ is described by a Walker DW profile, i.e., $\theta(z,t) = 2\arctan\{\exp[(z - \int_0^t v(\tau)d\tau)/\Delta(t)]\}$. This assumption allows us to compute $\frac{\partial\theta}{\partial z} = \frac{\sin\theta}{\Delta}$, $\frac{\partial^2\theta}{\partial z^2} = \frac{\sin\theta\cos\theta}{\Delta^2}$. (2) Spins inside the DW approximately lie in a plane during the DW propagation and periodic deformation of the DW structure. (3) A DW can adjust its structure to the change of magnetic anisotropy instantaneously during its precession as long as H is not more than $5H_W$. Thus the DW width Δ is $\Delta(t) = \sqrt{\frac{A}{K_z + K_y \sin^2\phi(t)}}$. Under these approximations ϕ does not depend on z such that $\frac{\partial\phi}{\partial z} = 0$, $\frac{\partial^2\phi}{\partial z^2} = 0$. G and $H_{\text{eff},\phi}$ become

$$G = \frac{2\sin\theta\cos\theta}{\mu_0(M_1 - M_2)}\left[\frac{A}{\Delta^2} - (K_z + K_y \sin^2\phi)\right], \tag{C6}$$

$$H_{\text{eff},\phi} = -\frac{1}{\mu_0(M_1 - M_2)\sin\theta}\frac{\partial f}{\partial \phi} = -\frac{K_y \sin 2\phi \sin\theta}{\mu_0(M_1 - M_2)}. \tag{C7}$$

$G \simeq 0$ since $\Delta(t) = \sqrt{\frac{A}{K_z + K_y \sin^2\phi}}$. In another word, G does not contribute to $\bar{v}$ in Eq. (C4). In later section, $G \simeq 0$ will be verified in our micromagnetic simulations.

The last term of Eq. (C4) can be recast as

$$\frac{c_1}{2\bar{\Delta}H}\overline{\int H_{\text{eff},\phi}^2 dz} = \frac{c_1}{\bar{\Delta}H}\frac{K_y^2\overline{\Delta\sin^2 2\phi}}{\mu_0^2(M_1 - M_2)^2} = \frac{c_1 H_W^2}{\alpha_{\rm eff}^2 H}\frac{\overline{\Delta\sin^2 2\phi}}{\bar{\Delta}}. \tag{C8}$$

To further simplify Eq. (C8), we use Eq. (11) in the main text to find $\phi(t)$ and its field dependence. Substituting expressions of $H_{\text{eff},\theta}$, $H_{\text{eff},\phi}$, $G \simeq 0$, and Walker breakdown field $H_W = \frac{\alpha_{\rm eff} K_y}{\mu_0(M_1 - M_2)}$ into Eq. (11) in the main text, we have

$$\left(1 + \alpha_{\rm eff}^2\right)\sin\theta\frac{\partial\phi}{\partial t} = \gamma_{\rm eff}(-H_W \sin 2\phi \sin\theta + H\sin\theta). \tag{C9}$$

Without losing generality, $M_1 - M_2 > 0$, $s_1 - s_2 > 0$ is assumed here. Multiply both side of Eq. (C9) by $\sin\theta$ and integrate over z, one has

$$\frac{\partial\phi}{\partial t} = \frac{\gamma_{\rm eff} H_W}{\left(1 + \alpha_{\rm eff}^2\right)}\left(\frac{H}{H_W} - \sin 2\phi\right). \tag{C10}$$

Equation (C10) has an analytical solution, in terms of dimensionless time $\tilde{t} = \frac{\gamma_{\rm eff} H_W}{(1+\alpha_{\rm eff}^2)}t$ and dimensionless field

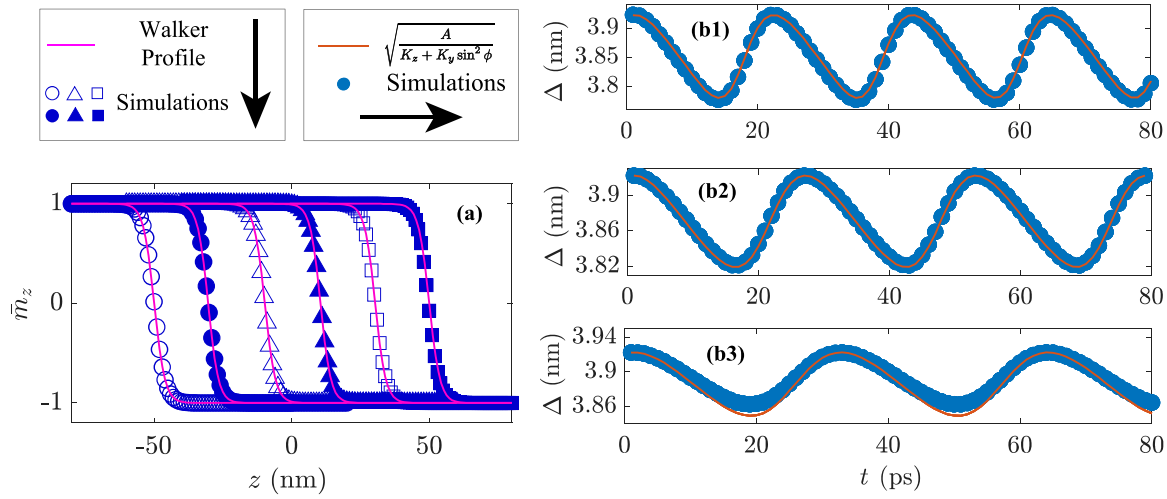

FIG. 5. (a) Spin profiles of DW for wires specified by Set 1 (circles), Set 2 (triangles), and Set 3 (squares) at $t = 8, 22$ ps (open and filled circles); $t = 19, 30$ ps (open and filled triangles); and $t = 32, 66$ ps (open and filled squares). The magnetic field is $\mu_0 H = 1$ T for Set 1, 0.8 T for Set 2, and 0.65 T for Set 3. $\bar{m}_z(z)$ is the averaged m_z of the top layer over the x direction. The solid curves are the Walker profile with the parameter at each given time. [(b1)–(b3)] Time evolution of DW width. The symbols are from simulations for Set 1 under $\mu_0 H = 1$ T (b1); Set 2 under $\mu_0 H = 0.8$ T (b2); and Set 3 under $\mu_0 H = 0.65$ T (b3). The solid curves are the DW width in the Walker solution, $\Delta(t) = \sqrt{\frac{A}{K_z + K_y \sin^2\phi}}$.

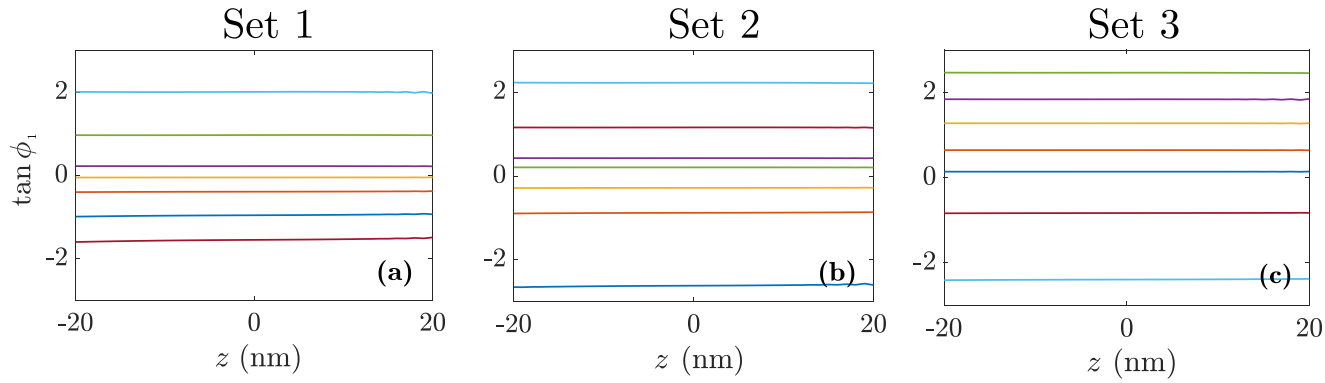

FIG. 6. $\tan\phi_1$ vs z. (a) Simulation results for Set 1 at $t = 60$ ps (orange), 70 ps (dark blue), 80 ps (yellow), 100 ps (violet), 150 ps (green), 180 ps (light blue), and 240 ps (crimson). (b) Simulation results for Set 2 at $t = 70$ ps (dark blue), 100 ps (orange), 130 ps (yellow), 170 ps (green), 190 ps (violet), 240 ps (crimson), and 270 ps (light blue). (c) Simulation results for Set 3 at $t = 70$ ps (dark blue), 120 ps (orange), 160 ps (yellow), 180 ps (violet), 580 ps (light blue), 620 ps (crimson), and 820 ps (green). Only DW region of [−20 nm, 20 nm] are shown with DW center shifted to $z = 0$. The magnetic field is $\mu_0 H = 1$ T for Set 1, 0.8 T for Set 2, and 0.65 T for Set 3.

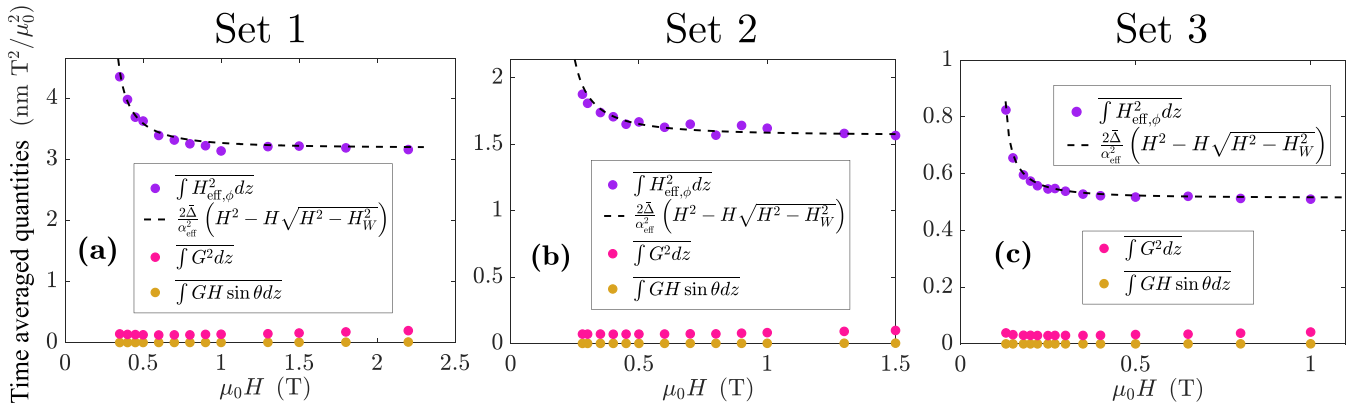

FIG. 7. Time averaged $\overline{\int H_{\text{eff},\phi}^2 dz}$ (violet circles), $\overline{\int G^2 dz}$ (pink circles), and $\overline{\int GH\sin\theta dz}$ (golden circles) from the spin configurations of MuMax3 simulations of DW motion in three wires specified by Set 1 (a), 2 (b), and 3 (c). $\overline{\int H_{\text{eff},\phi}^2 dz}$ accords well with the prediction of Eq. (C14) (dashed line) and the saturation values $\frac{\tilde{\Lambda}}{\alpha_{\text{eff}}^2} H_W^2$ are 3.18 nm T^2/μ_0^2 for (a), 1.57 nm T^2/μ_0^2 for (b), and 0.51 nm T^2/μ_0^2 for (c).

$h = \frac{H}{H_W} > 1$,

$$\phi(\tilde{t}) = \begin{cases} \arctan\left\{\frac{1+\sqrt{h^2-1}\tan\left[\sqrt{h^2-1}\tilde{t}-\arctan\left(\frac{1}{\sqrt{h^2-1}}\right)\right]}{h}\right\} & \tilde{t} \in [0, \tilde{t}_1) \\ \arctan\left\{\frac{1+\sqrt{h^2-1}\tan\left[\sqrt{h^2-1}\tilde{t}-\arctan\left(\frac{1}{\sqrt{h^2-1}}\right)\right]}{h}\right\} + n\pi & \tilde{t} \in [\tilde{t}_n, \tilde{t}_{n+1}),\ n = 1, 2, 3, \ldots \end{cases}, \tag{C11}$$

where $\tilde{t}_n = \frac{1}{\sqrt{h^2-1}}[\frac{(2n-1)\pi}{2} + \arctan(\frac{1}{\sqrt{h^2-1}})]$. ϕ is continuous and differentiable. The piecewise expression of ϕ is purely because arctangent function is defined in the range of $[-\frac{\pi}{2}, \frac{\pi}{2}]$. $\phi(t)$ for several choice of $h > 1$ are plotted in Fig. 4(a). Near critical value of $h = 1$, $\phi(t)$ shows a fast-slow motion and stays around $(n + 1/4)\pi$ (the plateaus) most of time. For $h \gg 1$, $\phi(t)$ increases linearly with time, showing a DW precession around wire axis at an almost constant angular velocity. Correspondingly, $\sin 2\phi(t)$ and $\cos 2\phi(t)$ deviate from the sine functions only for h not too larger than 1, but are almost perfect sine functions in time for $h = 5$ as shown in Fig. 4(b).

Equation (C11) enables us to analyze the field dependence of time averaged $\overline{\int H^2_{\text{eff},\phi} dz}$. The period of ϕ-precession is $\tilde{\mathcal{T}} = \frac{2\pi}{\sqrt{h^2-1}}$ in unit of $\frac{1+\alpha^2_{\text{eff}}}{\gamma_{\text{eff}} H_W}$. Define $k = K_y/K_z$ and let us first consider the limit case where $K_z \to \infty$ (i.e., $k \to 0$ but H_W is finite), then $\Delta = \bar{\Delta}$ in this limit. The time average of the right-hand side of Eq. (C8) is

$$\begin{aligned} \lim_{K_z \to +\infty} \frac{\overline{\Delta \sin^2 2\phi}}{\bar{\Delta}} \to \overline{\sin^2 2\phi} &= \frac{1}{\tilde{\mathcal{T}}} \int_0^{\tilde{\mathcal{T}}} \sin^2 2\phi d\tilde{t} = \frac{\sqrt{h^2-1}}{2\pi} \int_0^{2\pi} \frac{\sin^2 2\phi}{h - \sin 2\phi} d\phi \\ &= \frac{\sqrt{h^2-1}}{2\pi}\left(\frac{2\pi h^2}{\sqrt{h^2-1}} - 2\pi h\right) \\ &= h^2 - h\sqrt{h^2-1}. \end{aligned} \tag{C12}$$

$(h^2 - h\sqrt{h^2-1}) \to 1$ when $h \to 1$, which is the Walker breakdown threshold. $(h^2 - h\sqrt{h^2-1}) \to \frac{1}{2}$ when $h \to \infty$, an infinitely large field. For an arbitrary $h > 1$,

$$\frac{\overline{\Delta \sin^2 2\phi}}{\bar{\Delta}} = \frac{\int_0^{2\pi} \frac{\sin^2 2\phi}{(h-\sin 2\phi)\sqrt{1+k\sin^2\phi}} d\phi}{\int_0^{2\pi} \frac{1}{(h-\sin 2\phi)\sqrt{1+k\sin^2\phi}} d\phi}, \tag{C13}$$

are hard to evaluate analytically, but, surprisingly, it is very close to $h^2 - h\sqrt{h^2-1}$ for a wide range of k as shown in Fig 4(c). The numerical integrations of Eq. (C13) for various k ranging from 0.01 to 1 fall on the curve of $y = h^2 - h\sqrt{h^2-1}$.

With this approximate result, Eq. (C8) becomes

$$\frac{c_1}{2\bar{\Delta}H}\overline{\int H^2_{\text{eff},\phi} dz} = \frac{c_1 H_W^2}{\alpha^2_{\text{eff}} H}\left[\left(\frac{H}{H_W}\right)^2 - \frac{H}{H_W}\sqrt{\left(\frac{H}{H_W}\right)^2 - 1}\right] = \frac{c_1}{\alpha^2_{\text{eff}}}\left(H - \sqrt{H^2 - H_W^2}\right). \tag{C14}$$

Put all approximations together, the averaged DW velocity given in the main text is obtained

$$\bar{v} = c_1 H + \frac{c_1}{\alpha^2_{\text{eff}}}\left(H - \sqrt{H^2 - H_W^2}\right). \tag{C15}$$

APPENDIX D: VERIFICATION OF EXCELLENT APPROXIMATIONS IN APPENDIX C VIA SIMULATIONS

To verify excellent approximations used in deriving high-field velocity formula, we use MuMax3 [39] to solve the generic FiM dynamical equations [Eq. (2) in the main text] in a synthetic ferrimagnet [40] mentioned in Sec. IV.

1. Fast DW relaxation

We demonstrate below that the DW structure can follow the potential change during DW precession at least for $H < 5.5H_W$ used in our simulations. We show first analytically that DW relaxation is much faster than DW precession around the wire axis for $H < 5.5H_W$. Thus, G in $H_{\text{eff},\theta}$ has a negligible contribution to the average velocity. Then, we use MuMax3 to numerically obtain several snapshots of DW spin profile and the time-dependence of DW width and compare them with the Walker profile and theoretical DW width $\Delta(t) = \sqrt{\frac{A}{K_z + K_y \sin^2\phi(t)}}$, to valid whether a DW width can respond instantaneously to the potential change during the DW precession.

DW width $\Delta(t)$ is governed by the following equation [48]:

$$\frac{d\Delta}{dt} = \frac{12\gamma_{\text{eff}}}{\pi^2\mu_0(M_1 - M_2)\alpha_{\text{eff}}}\left[\frac{A}{\Delta} - \left(K_z + K_y \sin^2\phi\right)\Delta\right]. \tag{D1}$$

Using $\sqrt{\frac{A}{K_z}}$ and $[\frac{\pi^2\mu_0(M_1-M_2)\alpha_{\text{eff}}}{12\gamma_{\text{eff}}K_z}]$ as length and time units, Eq. (D1) can be written as

$$\frac{d\Delta}{dt} = \left\{\frac{1}{\Delta} - \Delta\left[1 + k\sin^2\phi(\xi t)\right]\right\}, \tag{D2}$$

where $\xi = [\frac{\pi^2\mu_0(M_1-M_2)\alpha_{\rm eff}}{12\gamma_{\rm eff}K_z}]/(\frac{1+\alpha_{\rm eff}^2}{\gamma_{\rm eff}H_W}) = \frac{\pi^2\alpha_{\rm eff}^2K_y}{12(1+\alpha_{\rm eff}^2)K_z}$ is the ratio between the relaxation time of DW width and typical time scale of ϕ motion, $k \equiv K_y/K_z$. In most cases, $\xi \ll 1$, thus we can treat $[1 + k\sin^2\phi(\xi t)]$ as a constant (adiabatic approximation), i.e., $\phi(t)$ is a slow motion compared to the relaxation of Δ. In this case, $\Delta \approx \sqrt{\frac{1+ke^{-2t[1+k\sin^2\phi(\xi t)]}\sin^2\phi(\xi t)}{1+k\sin^2\phi(\xi t)}}$. We choose $\xi \sim 0.01$ in the micromagnetic simulations presented here. We found no visible retardation in DW width as shown in Figs. 5(a) and 5(b1)–5(b3). The symbols in Fig. 5(a) are the snapshots of averaged $\bar{m}_z(z,t) = \frac{1}{16}\sum_{x=1,16} m_z(x,2,z,t)$ in the top layer for the wires specified by Set 1, 2, and 3 (squares) at several moments. The material parameters are listed in Table I, and applied magnetic field is $\mu_0 H = 1$ T for Set 1, 0.8 T for Set 2, and 0.65 T for Set 3.

The solid curves are the Walker DW profile of $\Delta(t) = \sqrt{\frac{A}{K_z+K_y\sin^2\phi}}$. The symbols in Figs. 5(b1)–5(b3) are $\Delta(t)$ directly obtained from MuMax3 simulations for wires denoted as Set 1 (b1), Set 2 (b2), and Set 3 (b3). The curves are $\Delta(t) = \sqrt{\frac{A}{K_z+K_y\sin^2\phi}}$. The overlap of simulation results and theoretical formula of both the Walker profile and $\Delta(t)$ demonstrates that DW width can follow the potential change.

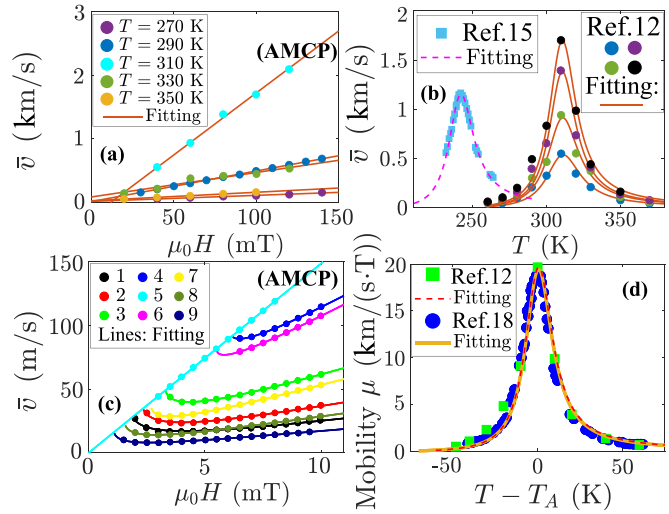

FIG. 8. Comparison of our theory with existing experiments and simulations. The symbols are experimental results from Refs. [12,15,18], and solid curves are theoretical fittings. (a) $\bar{v}$-$\mu_0 H$ relations at different temperatures. (b) $\bar{v}$-T relations under different magnetic fields. (c) Numerical simulations $\bar{v}$-$\mu_0 H$ relations for 9 sets of data extracted from Ref. [12]. (d) DW mobility at different temperatures around the AMCP.

2. Validity of DW-plane and internal field contributions to DW velocity

From MuMax3 simulations of wires labeled as Set 1, 2, and 3 mentioned above, we can numerically show that spins inside DW lie in a plane during its propagation and precession. In order to do so, we can compute $\phi_1(z,t) \equiv \frac{1}{32}\sum_{x=1,2,...,15,16}\sum_{y=1,2}\phi(x,y,z,t)$, where $\phi(x,y,z,t)$ is the azimuthal angle of magnetization in each cell labeled by (x,y,z) and at time t. Figure 6 are $\tan\phi_1(z,t)$ vs z at $t = 60, 70, 80, 100, 150, 180, 240$ ps for Set 1 (a), $t = 70, 100, 130, 170, 190, 240, 270$ ps for Set 2 (b), and $t = 70, 120, 160, 180, 580, 620, 820$ ps for Set 3 (c). The flat lines demonstrate that all spins lie indeed in a plane.

In order to numerically show that G does not contribute to $\bar{v}$ and $H_{{\rm eff},\phi}$ has an important contribution to the average DW velocity that leads to negative DW mobility, we also compute the time averaged $\overline{\int H_{{\rm eff},\phi}^2 dz}$, $\overline{\int G^2 dz}$, and $\overline{\int GH\sin\theta dz}$ under various magnetic fields using the spin configurations obtained from MuMax3 simulations for wires of Set 1, 2, and 3. The results are plotted in Figs. 7(a), 7(b), and 7(c) for Sets 1, 2, and 3, respectively. Indeed, $\overline{\int GH\sin\theta dz}$ is almost zero, and $\overline{\int G^2 dz}$ is negligibly small for all three wires. $\overline{\int H_{{\rm eff},\phi}^2 dz}$ accords well with the prediction of Eq. (C14) (dashed line) and the saturation value is $\frac{\tilde{\Delta}}{\alpha_{\rm eff}^2}H_W^2$. In summary, all the assumptions we made in Sec. C 2 are valid.

APPENDIX E: COMPARISON OF THEORY, EXISTING EXPERIMENTS, AND SIMULATIONS

In this section, we compare our theory with existing experiments [12,15,18] and simulations [12] in the literature. The data are extracted from the original figures in Refs. [12,15,18] using an online digitization tool WebPlotDigitizer [49]. All the experiments are done at high external magnetic fields far above the Walker breakdown ($\mu_0 H \gg \mu_0 H_W$), thus we use the high field limit of Eq. (12) to fit the experimental data.

Figure 8(a) is the velocity-magnetic field relation at different temperatures given in [12]. We use $\bar{v} = c_1 H + v_d$ to fit the data (circles), where c_1 is the DW mobility at high field limit, v_d is a correction velocity, taking into account the pinning effects, thermal fluctuations, and other detection inaccuracies. For $T = 270, 290, 310, 330, 350$ K, we have $c_1 = 0.945, 4.807, 19.490, 3.846, 1.335\,\mu_0$ km s^{-1}T^{-1}, $v_d = 19.28, 15.75, -226.60, 88.28, 29.02$ m/s respectively. The fitting results are shown by the solid lines. The angular momentum compensation temperature T_A is 310 K.

Figure 8(b) shows the comparison of our theory with the velocity-temperature relation under different magnetic fields given in Ref. [12] (circles) and Ref. [15] (squares). Recalling the expression of $c_1 = \frac{(M_1-M_2)\alpha\tilde{\Delta}}{(s_1-s_2)^2+\alpha^2}$, in order to convert it to the temperature dependence, we assume that, in the vicinity of T_A, $(s_1 - s_2) \propto (T - T_A)$, and $M_{\rm eff}(T) = M_1(T) - M_2(T)$ is linear in T, these assumptions are indeed valid according to the information given in Refs. [12,15]. Thus we use $\bar{v} = \frac{C_0 M_{\rm eff}(T)}{(T-T_A)^2+T_0^2}\mu_0 H$ to fit the $v - T$ curve, where $M_{\rm eff}(T)$ is obtained from another linear fitting of the net magnetization data, T_A and $\mu_0 H$ are known from the experimental condition, and C_0 and T_0 are two fitting parameters. The blue, green, purple, and black circles coming from Ref. [12] correspond to $\mu_0 H = 40, 60, 80, 100$ mT respectively, with $C_0 = 61.1718, 57.5517, 47.4968, 48.2884$ m^{2}K^{2}s^{-1}T^{-1}A^{-1}, and $T_0 = 14.1216, 12.8628, 10.9641, 11.1489$ K, where $T_A = 310$ K, $M_{\rm eff}(T) = [593.8({\rm K}^{-1})\,T - 140600]$ A/m. The fitting results are given by the solid curves. The light blue squares coming from Ref. [15] correspond to $\mu_0 H = 85$ mT,

which gives $C_0 = 56.28\,\mathrm{m^2K^2s^{-1}T^{-1}A^{-1}}$, $T_0 = 10.31\,\mathrm{K}$, where $T_A = 241\,\mathrm{K}$, and $M_{\mathrm{eff}}(T) = [489.3(\mathrm{K}^{-1})\,T - 92550]$ A/m. The fitting result is shown by magenta dashed curve.

Figure 8(c) shows a comparison of our theory (solid line) and the numerical simulation results for $H > H_W$ in Ref. [12] (circles). We use Eq. (12) to fit the data, treating c_1 and α_{eff} as fitting parameters. The dataset indices 1–9 are exactly the same as the in Ref. [12], The Walker breakdown fields of dataset 1, 2, 3, 4, 6, 7, 8, 9 are known as $\mu_0 H_W$ = 1.7112, 2.2635, 3.2816, 6.1191, 5.5126, 2.6859, 1.5300,1.0600 mT, The respective fitting parameters are c_1 = 2.1980, 3.2770, 5.5830, 10.3700, 9.9560, 5.0040, 2.6860, 1.6190 μ_0 km $\mathrm{s^{-1}T^{-1}}$, and α_{eff} = 0.3186, 0.4614, 0.7298, 1.4190, 1.4380, 0.7493, 0.4311, 0.3090. For dataset 5, which is at AMCP, we use $\bar{v} = c_1 H$ to fit, a larger mobility $c_1 = 14.8700\,\mu_0$ $\mathrm{km\,s^{-1}T^{-1}}$ is obtained.

Figure 8(d) shows the mobility-temperature relation given in Ref. [12,18], compared to a fitting based on our theoretical result of mobility $\mu = \frac{C_0 M_{\mathrm{eff}}(T)}{(T-T_A)^2+T_0^2}$. The green squares are from Ref. [12], with $C_0 = 43.10\,\mathrm{m^2K^2s^{-1}T^{-1}A^{-1}}$ and $T_0 = 9.78\,\mathrm{K}$, compared to the red dashed line (fitting). The $M_{\mathrm{eff}}(T)$ here is same as Fig. 8(b). The blue circles are results of Ref. [18], with $C_0 = 42.82\,\mathrm{m^2K^2s^{-1}T^{-1}A^{-1}}$ and $T_0 = 9.66\,\mathrm{K}$, where $M_{\mathrm{eff}}(T) = [544.3(\mathrm{K}^{-1})\,T + 42190]$ A/m. The fitting result is shown by the golden-solid curve.

[1] B. Hu and X. R. Wang, Instability of Walker Propagating Domain Wall in Magnetic Nanowires, Phys. Rev. Lett. **111**, 027205 (2013).

[2] X. S. Wang, P. Yan, Y. H. Shen, G. E. W. Bauer, and X. R. Wang, Domain Wall Propagation through Spin Wave Emission, Phys. Rev. Lett. **109**, 167209 (2012).

[3] E. G. Galkina and B. A. Ivanov, Dynamic solitons in antiferromagnets (Review Article), Low Temp. Phys. **44**, 618 (2018).

[4] V. G. Bar'yakhtar, B. A. Ivanov, and M. V. Chetkin, Dynamics of domain walls in weak ferromagnets, Sov. Phys. Usp. **28**, 563 (1985).

[5] A. M. Kosevich, B. A. Ivanov, and A. S. Kovalev, Magnetic solitons, Phys. Rep. **194**, 117 (1990).

[6] S. S. P. Parkin, M. Hayashi, and L. Thomas, Magnetic domain-wall racetrack memory, Science **320**, 190 (2008).

[7] N. L. Schryer and L. R. Walker, The motion of 180° domain walls in uniform dc magnetic fields, J. Appl. Phys. **45**, 5406 (1974).

[8] V. Baltz, A. Manchon, M. Tsoi, T. Moriyama, T. Ono, and Y. Tserkovnyak, Antiferromagnetic spintronics, Rev. Mod. Phys. **90**, 015005 (2018).

[9] O. Gomonay, T. Jungwirth, and J. Sinova, High Antiferromagnetic Domain Wall Velocity Induced by Néel Spin-Orbit Torques, Phys. Rev. Lett. **117**, 017202 (2016).

[10] S.-H. Yang, K.-S. Ryu, and S. Parkin, Domain-wall velocities of up to 750ms^{-1} driven by exchange-coupling torque in synthetic antiferromagnets, Nat. Nanotechnol. **10**, 221 (2015).

[11] S. K. Kim, G. S. D. Beach, K.-J. Lee, T. Ono, T. Rasing, and H. Yang, Ferrimagnetic spintronics, Nat. Mater. **21**, 24 (2022).

[12] K.-J. Kim, S. K. Kim, Y. Hirata, S.-H. Oh, T. Tono, D.-H. Kim, T. Okuno, W. S. Ham, S. Kim, G. Go *et al.*, Fast domain wall motion in the vicinity of the angular momentum compensation temperature of ferrimagnets, Nat. Mater. **16**, 1187 (2017).

[13] L. Caretta, M. Mann, F. Büttner, K. Ueda, B. Pfau, C. M. Günther, P. Hessing, A. Churikova, C. Klose, M. Schneider *et al.*, Fast current-driven domain walls and small skyrmions in a compensated ferrimagnet, Nat. Nanotechnol. **13**, 1154 (2018).

[14] S. A. Siddiqui, J. Han, J. T. Finley, C. A. Ross, and L. Liu, Current-Induced Domain Wall Motion in a Compensated Ferrimagnet, Phys. Rev. Lett. **121**, 057701 (2018).

[15] T. Okuno, D.-H. Kim, S.-H. Oh, S. K. Kim, Y. Hirata, T. Nishimura, W. S. Ham, Y. Futakawa, H. Yoshikawa, A. Tsukamoto *et al.*, Spin-transfer torques for domain wall motion in antiferromagnetically coupled ferrimagnets, Nat. Electron. **2**, 389 (2019).

[16] K. Cai, Z. Zhu, J. M. Lee, R. Mishra, L. Ren, S. D. Pollard, P. He, G. Liang, K. L. Teo, and H. Yang, Ultrafast and energy-efficient spin-orbit torque switching in compensated ferrimagnets, Nat. Electron. **3**, 37 (2020).

[17] E. Haltz, J. Sampaio, S. Krishnia, L. Berges, R. Weil, and A. Mougin, Measurement of the tilt of a moving domain wall shows precession-free dynamics in compensated ferrimagnets, Sci. Rep. **10**, 16292 (2020).

[18] D.-H. Kim, T. Okuno, S. K. Kim, S.-H. Oh, T. Nishimura, Y. Hirata, Y. Futakawa, H. Yoshikawa, A. Tsukamoto, Y. Tserkovnyak, Y. Shiota, T. Moriyama, K.-J. Kim, K.-J. Lee, and T. Ono, Low Magnetic Damping of Ferrimagnetic GdFeCo Alloys, Phys. Rev. Lett. **122**, 127203 (2019).

[19] M. V. Logunov, S. S. Safonov, A. S. Fedorov, A. A. Danilova, N. V. Moiseev, A. R. Safin, S. A. Nikitov, and A. Kirilyuk, Domain Wall Motion Across Magnetic and Spin Compensation Points in Magnetic Garnets, Phys. Rev. Appl. **15**, 064024 (2021).

[20] V. V. Yurlov, K. A. Zvezdin, P. N. Skirdkov, and A. K. Zvezdin, Domain wall dynamics of ferrimagnets influenced by spin current near the angular momentum compensation temperature, Phys. Rev. B **103**, 134442 (2021).

[21] W. H. Li, Z. Jin, D. L. Wen, X. M. Zhang, M. H. Qin, and J. M. Liu, Ultrafast domain wall motion in ferrimagnets induced by magnetic anisotropy gradient, Phys. Rev. B **101**, 024414 (2020).

[22] M. Jin, I.-S. Hong, D.-H. Kim, K.-J. Lee, and S. K. Kim, Domain-wall motion driven by a rotating field in a ferrimagnet, Phys. Rev. B **104**, 184431 (2021).

[23] S.-H. Oh, S. K. Kim, J. Xiao, and K.-J. Lee, Bidirectional spin-wave-driven domain wall motion in ferrimagnets, Phys. Rev. B **100**, 174403 (2019).

[24] E. Haltz, S. Krishnia, L. Berges, A. Mougin, and J. Sampaio, Domain wall dynamics in antiferromagnetically coupled double-lattice systems, Phys. Rev. B **103**, 014444 (2021).

[25] A. K. Zvezdin, Z. V. Gareeva, and K. A. Zvezdin, Anomalies in the dynamics of ferrimagnets near the angular momentum compensation point, J. Magn. Magn. Mater. **509**, 166876 (2020).

[26] E. Martínez, V. Raposo, and Ó. Alejos, Novel interpretation of recent experiments on the dynamics of domain walls along ferrimagnetic strips, J. Phys.: Condens. Matter **32**, 465803 (2020).

[27] B. A. Ivanov, E. G. Galkina, V. E. Kireev, N. E. Kulagin, R. V. Ovcharov, and R. S. Khymyn, Nonstationary forced motion of domain walls in ferrimagnets near the spin compensation point, Low Temp. Phys. **46**, 841 (2020).

[28] A. A. Thiele, Steady-State Motion of Magnetic Domains, Phys. Rev. Lett. **30**, 230 (1973).

[29] H. Y. Yuan, Q. Liu, K. Xia, Z. Yuan, and X. R. Wang, Proper dissipative torques in antiferromagnetic dynamics, Europhys. Lett. **126**, 67006 (2019).

[30] A. Kamra, R. E. Troncoso, W. Belzig, and A. Brataas, Gilbert damping phenomenology for two-sublattice magnets, Phys. Rev. B **98**, 184402 (2018).

[31] T. L. Gilbert, A phenomenological theory of damping in ferromagnetic materials, IEEE Trans. Magn. **40**, 3443 (2004).

[32] V. G. Baryakhtar, B. A. Ivanov, A. L. Sukstanskii, and E. Y. Melikhov, Soliton relaxation in magnets, Phys. Rev. B **56**, 619 (1997).

[33] R. K. Wangsness, Sublattice effects in magnetic resonance, Phys. Rev. **91**, 1085 (1953).

[34] M. Binder, A. Weber, O. Mosendz, G. Woltersdorf, M. Izquierdo, I. Neudecker, J. R. Dahn, T. D. Hatchard, J.-U. Thiele, C. H. Back, and M. R. Scheinfein, Magnetization dynamics of the ferrimagnet CoGd near the compensation of magnetization and angular momentum, Phys. Rev. B **74**, 134404 (2006).

[35] C. D. Stanciu, A. V. Kimel, F. Hansteen, A. Tsukamoto, A. Itoh, A. Kirilyuk, and T. Rasing, Ultrafast spin dynamics across compensation points in ferrimagnetic GdFeCo: The role of angular momentum compensation, Phys. Rev. B **73**, 220402(R) (2006).

[36] Z. Z. Sun and X. R. Wang, Strategy to reduce minimal magnetization switching field for Stoner particles, Phys. Rev. B **73**, 092416 (2006).

[37] X. R. Wang, P. Yan, J. Lu, and C. He, Magnetic field driven domain-wall propagation in magnetic nanowires, Ann. Phys. **324**, 1815 (2009).

[38] X. R. Wang, P. Yan, and J. Lu, High-field domain wall propagation velocity in magnetic nanowires, Europhys. Lett. **86**, 67001 (2009).

[39] A. Vansteenkiste, J. Leliaert, M. Dvornik, M. Helsen, F. G. Sanchez, and B. V. Waeyenberge, The design and verification of MuMax3, AIP Adv. **4**, 107133 (2014).

[40] R. A. Duine, K.-J. Lee, S. S. P. Parkin, and M. D. Stiles, Synthetic antiferromagnetic spintronics, Nat. Phys. **14**, 217 (2018).

[41] I. Radu, K. Vahaplar, C. Stamm, T. Kachel, N. Pontius, H. A. Dürr, T. A. Ostler, J. Barker, R. F. L. Evans, R. W. Chantrell *et al.*, Transient ferromagnetic-like state mediating ultrafast reversal of antiferromagnetically coupled spins, Nature (London) **472**, 205 (2011).

[42] C. E. Patrick, S. Kumar, G. Balakrishnan, R. S. Edwards, M. R. Lees, L. Petit, and J. B. Staunton, Calculating the Magnetic Anisotropy of Rare-Earth–Transition-Metal Ferrimagnets, Phys. Rev. Lett. **120**, 097202 (2018).

[43] M. Ding and S. J. Poon, Tunable perpendicular magnetic anisotropy in GdFeCo amorphous films, J. Magn. Magn. Mater. **339**, 51 (2013).

[44] H. Damas, A. Anadon, D. C. Berrocal, J. A. Saenz, J. Bello, A. A. Córdova, S. Migot, J. Ghanbaja, O. Copie, M. Hehn *et al.*, Ferrimagnet GdFeCo characterization for spin-orbitronics: Large field-like and damping-like torques, Phys. Status Solidi RRL **16**, 2200035 (2022).

[45] T. Ono, H. Miyajima, K. Shigeto, K. Mibu, N. Hosoito, and T. Shinjo, Propagation of a magnetic domain wall in a submicrometer magnetic wire, Science **284**, 468 (1999).

[46] G. S. D. Beach, C. Nistor, C. Knutson, M. Tsoi, and J. L. Erskine, Dynamics of field-driven domain-wall propagation in ferromagnetic nanowires, Nat. Mater. **4**, 741 (2005).

[47] H. Goldstein, C. P. Poole, and J. L. Safko, *Classical Mechanics*, 3rd Edition (Addison-Wesley, New York, 2002).

[48] B. Hillebrands, A. Thiaville (Editors), *Spin Dynamics in Confined Magnetic Structures III*, (Springer-Verlag, Berlin, 2006).

[49] A. Rohatgi, WebPlotDigitizer: Version 4.6 (2022).